

Automatic 3D illumination-diagnosis method for large- N arrays: Robust data scanner and machine-learning feature provider

Michał Chamarczuk¹, Michał Malinowski¹, Yohei Nishitsuji², Jan Thorbecke³, Emilia Koivisto⁴, Suvi Heinonen⁵, Sanna Juurela⁶, Miłosz Mężyk¹, and Deyan Draganov³

ABSTRACT

The main issues related to passive-source reflection imaging with seismic interferometry (SI) are inadequate acquisition parameters for sufficient spatial wavefield sampling and vulnerability of surface arrays to the dominant influence of the omnipresent surface-wave sources. Additionally, long recordings provide large data volumes that require robust and efficient processing methods. We address these problems by developing a two-step wavefield evaluation and event detection (TWEED) method of body waves in recorded ambient noise. TWEED evaluates the spatiotemporal characteristics of noise recordings by simultaneous analysis of adjacent receiver lines. We test our method on synthetic data representing transient ambient-noise sources at the surface and in the deeper subsurface. We discriminate between basic types of seismic events by using three adjacent receiver lines. Subsequently, we apply TWEED to 600 h

of ambient noise acquired with an approximately 1000-receiver array deployed over an active underground mine in Eastern Finland. We develop the detection of body-wave events related to mine blasts and other routine mining activities using a representative 1 h noise panel. Using TWEED, we successfully detect 1093 body-wave events in the full data set. To increase the computational efficiency, we use slowness parameters derived from the first step of TWEED as input to a support vector machine (SVM) algorithm. Using this approach, we detect 94% of the TWEED-evaluated body-wave events indicating the possibility to limit the illumination analysis to only one step, and therefore increase the time efficiency at the price of lower detection rate. However, TWEED on a small volume of the recorded data followed by SVM on the rest of the data could be efficiently used for a quick and robust (real-time) scanning for body-wave energy in large data volumes for subsequent application of SI for retrieval of reflections.

INTRODUCTION

In the past decade, the concept of seismic reflection imaging using ambient noise and seismic interferometry (SI) has emerged as a possible alternative for classic active-source surveys (Draganov and Ruigrok, 2015), in which the use of active sources is not feasible or is undesirable. In particular, passive-source SI provides an alternative when the terrain access or the budget is limited with regard to

using active sources. At the same time, acquisition of large- N arrays (i.e., arrays consisting of large number of sensors and short receiver spacing compared with the dominant wavelength) (Freed, 2008) is becoming popular in passive seismic experiments for long-period (large- T) recording of ambient seismic noise (Hansen and Schmandt, 2015; Li et al., 2018b). Some notable examples of deployed large- N arrays include the Long Beach nodal array (Lin et al., 2013), the San Jacinto array (Ben-Zion et al., 2015), the Malargüe array

Manuscript received by the Editor 2 July 2018; revised manuscript received 16 December 2018; published ahead of production 01 February 2019; published online 13 March 2019.

¹Institute of Geophysics PAS, Ksiecia Janusza 64, Warsaw 01-452, Poland. E-mail: mchamarczuk@igf.edu.pl; michalm@igf.edu.pl; mmezyk@igf.edu.pl.

²Delft University of Technology, Faculty of Civil Engineering and Geosciences, Stevinweg 1, PO Box 5048, Delft NL 2628 CN, Netherlands and Petro Summit E&P Corporation, 3-2 Otemachi 2-Chome, Chiyoda-ku, Tokyo 100-8601, Japan. E-mail: y.nishitsuji@tudelft.nl.

³Delft University of Technology, Faculty of Civil Engineering and Geosciences, Stevinweg 1, PO box 5048, Delft NL 2628 CN, Netherlands. E-mail: j.w.thorbecke@tudelft.nl; d.s.draganov@tudelft.nl.

⁴University of Helsinki, Department of Geosciences and Geography, Gustaf Hällströmin katu 2b, Helsinki, Finland. E-mail: emilia.koivisto@helsinki.fi.

⁵Geological Survey of Finland, PO Box 96, Espoo 02150, Finland. E-mail: suvi.heinonen@gtk.fi.

⁶Boliden FinnEx Oy, Kevitsantie 730, Petkula 99670, Finland. E-mail: sanna.juurela@boliden.com.

© 2019 Society of Exploration Geophysicists. All rights reserved.

(Ruigrok et al., 2012; Nishitsuji et al., 2014), the Diablo Canyon array (Nakata and Beroza, 2017), and the Mount St. Helens array (Hansen and Schmandt, 2015).

Large- N arrays create opportunity for 3D reflection imaging in challenging field areas (Ruigrok et al., 2012). Similar to other exploration methods, the most interesting part of the wavefield for imaging purposes are the reflected body waves, which carry information about the sharp impedance contrasts in the subsurface (Brennguier et al., 2016). One way of imaging the earth's interior using P-waves is SI. To successfully apply SI, one needs body-wave arrivals to be present in the recorded noise (Draganov et al., 2013). Unfortunately, body waves present in ambient-noise recordings are usually masked by dominant surface waves (Draganov et al., 2009). Hence, the quality of the retrieved subsurface image strongly depends on how well we are able to extract the desired body waves from the ambient noise in the recording area. Examples of successful imaging with body-wave SI include reflection imaging in a desert area in Libya (Draganov et al., 2009, 2013), a passive seismic experiment for mineral exploration at Lalor Lake, Manitoba (Cheraghi et al., 2015), ambient-noise body-wave tomography at Long Beach, California (Lin et al., 2013; Nakata et al., 2015), and S-wave tomography in an underground mine (Olivier et al., 2015). Each of these experiments was conducted in different terrain and aimed to image different structural targets, yet the inherent processing is based upon selective stacking of ambient-noise data. Draganov et al. (2013) and Cheraghi et al. (2015) use directional analysis and surface-wave suppression with a band-pass filter for selective stacking, whereas Olivier et al. (2015) directly analyze the signal-to-noise ratio (S/N) of the desired arrivals in the correlated panels. In their ambient-noise body-wave tomography study, Nakata et al. (2015) combine selective stacking with coherency filtering. In the following study, we develop a robust detection method that identifies body-wave arrivals to serve as the input for further reflection imaging. Furthermore, we evaluate the quantitative metrics of basic ambient-noise source types present in large passive data sets.

Seismic acquisition patterns depend on the aim of the survey. At the exploration scale, one of the most common acquisition layouts is the orthogonal one, in which the source and receiver lines are more or less perpendicular to each other, with line spacing that usually exceeds the receiver spacing by an order of magnitude (Meunier, 2011). In this case, the receiver sampling in the crossline direction is not adequate to fully resolve the wavelengths typical for an exploration seismic survey, which results in aliased wavefields between the receiver lines in the case of sparse sources (Chaouch and Mari, 2006). In such cases, it is difficult to remove scattered surface-wave noise from conventional surveys. Spatial aliasing is also a serious problem in many imaging techniques (e.g., migration; see Gray, 2013), but it can be remedied to some extent with, for example, data-regularization and interpolation techniques (Trad, 2009).

Insufficient crossline receiver spacing also constitutes a problem in passive seismic experiments because it hinders the beam-forming analysis (Brennguier et al., 2016) or limits the maximum available resolution for imaging with ambient-noise sources (Draganov et al., 2013; Quiros et al., 2017). In this paper, we aim to enhance the 3D imaging potential of already deployed large- N arrays with sparse crossline receiver sampling by developing an automatic detection of seismic body-wave events because, in the SI process, they contribute to the retrieval of reflections.

Using large- N arrays for long passive-recording campaigns creates demand for the development of robust and efficient ways to analyze

huge ambient-noise data sets (Hansen and Schmandt, 2015). These involve QC methods (McNamara et al., 2009), processing techniques (Bensen et al., 2007), and different detection methods (Yoon et al., 2015; Li et al., 2018b). The latter aim to extract portions of the recorded wavefield characterized by common metrics. For ambient-noise processing methods, some effective solutions are beam forming (Rost and Thomas, 2002), illumination diagnosis (Almagro Vidal et al., 2014; Panea et al., 2014), coherency filtering (Nakata et al., 2015), selective stacking (Nakata et al., 2015; Olivier et al., 2015), and filtering based on singular-value decomposition (SVD) (Melo et al., 2013; Moreau et al., 2017). In terms of detection methods, some interesting examples include source-scanning algorithms (Kao and Shan, 2004), template matching (Shelly et al., 2007), the short-term averaging (STA)/long-term averaging (LTA) technique (Allen, 1978), the fuzzy-logic method (Cercione, 1993), and a recently developed local-similarity approach (Li et al., 2018b) allowing detection of very weak events recorded with large- N arrays.

This distinction between processing and detection methods is somewhat artificial. For instance, reflection imaging with passive SI involves suppressing the surface waves, which can be achieved using methods emerging from both categories. These can include selecting parts of the wavefield using a variety of beam-forming methods: plane-wave beam forming (Draganov et al., 2013), spherical beam forming (Johnson and Dudgeon, 1993; Roots et al., 2017), double beam forming (Nakata et al., 2016; Roux et al., 2016), multi-rate beam forming (Corciulo et al., 2012), the MUSIC spectral method (Yunhuo et al., 2018), and selective-stacking algorithms (Nakata et al., 2015; Olivier et al., 2015). Beam forming combined with other filtering techniques, such as SVD can be used for enhancing the S/N of recorded arrivals or to detect the weak seismic events originally obscured by noise (Corciulo et al., 2012). Similarly, selective-stacking techniques are essentially detection methods, which, depending on the S/N in the desired arrival-time window evaluated on crosscorrelated data, reject the unnecessary parts of the ambient-noise wavefield. Therefore, a detection method can also be thought of as (1) a processing technique that filters out the undesired parts of the wavefield and (2) as a QC method that provides quantitative metrics about the whole data set. An example of such a tool is the InterLoc method proposed by Dales et al. (2017), in which a beam forming-like approach is used to analyze the noise-correlation functions obtained from an underground network of receivers to detect seismic events induced by underground mine activity.

Another effective way to extract body-wave arrivals from ambient-noise recordings is the illumination-diagnosis method introduced by Almagro Vidal et al. (2014), which requires acquisition with receivers that are sufficiently well spaced in the inline and crossline directions, e.g., having two or more crossing lines with the same or sufficient spacing along the lines. This method is closely related to beam forming. In beam forming, the average illumination along the receiver array is analyzed, whereas in illumination diagnosis, the analysis is done exactly at the location of a virtual source, thus increasing its ability to detect events recorded with a selected subset of a seismic array. The illumination-diagnosis method has already been successfully applied to ambient-noise recordings (Panea et al., 2014; Cheraghi et al., 2017). However, in both cases, two orthogonal receiver lines were available, which allowed for the discrimination between body and surface-wave events. In this paper, we investigate the possibility of applying illumination diagnosis when the receiver spacing

in the crossline direction is relatively coarse (i.e., as in conventional land 3D seismic surveys). We propose two-step wavefield evaluation and event detection (TWEED), which is designed to overcome the insufficient crossline receiver spacing by simultaneous analysis along several parallel receiver lines. In this sense, TWEED is a new implementation of the illumination-diagnosis method of [Almagro Vidal et al. \(2014\)](#) that is less demanding on the acquisition geometry because it does not require sufficient sampling in the crossline direction.

Although detection of body-wave events is beneficial for imaging with SI, we also identify other areas where such detected events might contribute as valuable input, such as microseismic imaging ([Reshetnikov et al., 2010](#)), reverse vertical seismic profiling using ambient noise ([Quiros et al., 2017](#)), monitoring mine activity ([Dales et al., 2017](#)), and reflection tomography ([Jousset et al., 2016](#)). In fact, any huge ambient-noise data set can be scanned for the desired type of seismic events, when more than one receiver line is available.

We demonstrate the effectiveness of the TWEED method on the synthetic and field data. The field data are one month of continuous ambient-noise recordings from a large- N array deployed in the Kylylahti area, Eastern Finland, where an active underground mine is operated by Boliden. Furthermore, motivated by the recent examples of effective applications of machine-learning techniques to ambient-noise data sets ([Li et al., 2018a](#)) and active-source data in an underground mine ([Olivier et al., 2018](#)), we investigate the feasibility of machine learning in the detection of body-wave events. Our aim is to develop an efficient and robust automatic detection method; therefore, we examine the possibility of replacing the second step in TWEED by an support vector machine (SVM) classifier with the aim to improve the time efficiency of the body-wave detection.

First, we introduce the theory underlying our detection method and describe TWEED as an extension of the technique introduced by [Almagro Vidal et al. \(2014\)](#) to 3D along separate lines. We show the results of applying TWEED on synthetic 3D data simulating two cases of transient sources: a source at the surface (generating primarily surface-wave energy) and a source placed deeper in the subsurface (giving rise primarily to body-wave energy). By comparing the results obtained with our method for these two cases, we show the necessity of the second step in TWEED. Subsequently, we apply our method to the ambient-noise data recorded over the Kylylahti mine. We evaluate the detection along three adjacent receiver lines deployed in a spatial configuration very similar to the synthetic experiment. In the final section, we test the SVM technique on the same data set and compare it with the results obtained with TWEED, with the latter considered as the ground truth in this case. For the SVM, we use slowness values obtained exclusively from the first step of TWEED as input features. Finally, based on the results obtained using TWEED and SVM, we highlight the potential practical applications for both methods.

THEORY OF TWEED

A single ambient-noise event can be considered as a group of transient waveforms radiated from a localized natural or man-made seismic source ([Bormann, 1998](#)). If such sources are acting separately in time, they can be effectively recorded and divided into short recording segments called panels. Illumination characteristics of a transient source can be studied in a virtual common-source panel ([van der Neut et al., 2011](#); [Almagro Vidal et al., 2014](#)), which can be described as

$$C^S(\mathbf{x}_B, \mathbf{x}_A, t) = \frac{1}{\rho c} (u^{\text{obs}}(x_A, x_S, -t) * u^{\text{obs}}(x_B, x_S, t)), \quad (1)$$

as if a source were located at receiver \mathbf{x}_A that emits energy within a limited window of angles to multiple receivers \mathbf{x}_B , where ρ and c are the constant mass density and velocity of the medium at and outside ∂D , respectively; $*$ denotes time convolution; and $u^{\text{obs}}(x_A, x_S, -t)$ is the time-reversed wavefield observed at \mathbf{x}_A due to a transient source at x_S . The ray parameter of the event passing through time $t = 0$ s at the location of receiver x_A (master trace, i.e., the virtual-source location) provides a measure of the illumination characteristics of the dominant transient source captured in a given noise panel. Therefore, this ray parameter is a potential tool to discriminate between different types of seismic events, e.g., between surface and body waves. An efficient way to evaluate the ray parameter is the slant-stack transform ([Chapman, 1981](#)). In a noise panel recorded by a single receiver line, surface- and body-wave events could be recorded as wavefronts with high apparent velocity (see [Figure 1a](#)). To distinguish between these two types of events, we introduce TWEED. In the first step, we use the slant-stack transform of field v , $\tilde{v}(p, \tau) = \int v(x, \tau + px) dx$, where p is the ray parameter, x is the offset, and τ is the intercept time at $p = 0$. We evaluate the slant stack at $\tau = 0$ s for each virtual common-source panel C^S :

$$\tilde{C}^S(\mathbf{x}_A, \mathbf{p}) = \int C^S[x_B, x_A, \mathbf{p} \cdot (x_B - x_A)] dx_B, \quad (2)$$

where \tilde{C}^S is the representation of the virtual-source function of the transient source S in the τ - p domain. Therefore, \tilde{C}^S describes the dominant ray-parameter contribution from the transient source to the virtual source located at x_A and recorded at x_B . Then, a discrimination test is performed by comparing the dominant ray-parameter value $\max(\|\tilde{C}_L^S(x_A, \mathbf{p})\|)$ with the predefined ray-parameter threshold p_{limit} :

$$C_L^S(\mathbf{x}_B, \mathbf{x}_A, t) = \begin{cases} 0 & \text{if } \max(\|\tilde{C}_L^S(x_A, \mathbf{p})\|) > p_{\text{limit}} \\ \frac{1}{\rho c} (u^{\text{obs}}(x_A, x_S, -t) * u^{\text{obs}}(x_B, x_S, t)) & \text{if } \max(\|\tilde{C}_L^S(x_A, \mathbf{p})\|) \leq p_{\text{limit}} \end{cases}, \quad (3)$$

where p_{limit} is the expected minimum value of the P-wave slowness in the recording area. Note that the only difference of the first step of this method and the one introduced by [Almagro Vidal et al. \(2014\)](#) is that for a given time period, we perform this analysis on noise panels recorded simultaneously at several parallel recording lines, indicated by the subscript L , instead of a single receiver line, hence extending this illumination analysis to 3D surveys along separate lines. In the second step, we use the observation that a body-wave event arriving at the recording array from below should be recorded by several receiver lines with a time difference much smaller than that expected for surface waves. In general, this time difference would go to zero as the wavefront approaches the shape of a vertical plane wave. Because we are interested in the arrival time of an event, the second step is evaluated on noise panels in the time domain. In this step, we scan the noise panels using a sliding time window. We evaluate the ray parameter of the dominant event within each time window and determine the event with the highest slant-stack value for the whole panel. Given the difference of arrival times Δt_i for this event from the i th parallel receiver line, and the distance between them Δx_i , the apparent slowness \mathbf{p}_{c_i} in the crossline direction is estimated:

$$p_{cl} = \frac{\Delta t_i}{\Delta x_i} \tag{4}$$

Depending on the predefined body-wave velocity limit, a decision about the type of event is made:

$$U_L^{obs}(t) = \begin{cases} 0, & \text{if } p_{c1} \wedge p_{c2} > p_{limit}, \\ u_{body}^{obs} & \text{if } p_{c1} \wedge p_{c2} \leq p_{limit}, \end{cases} \tag{5}$$

where \wedge represents the logical conjunction (the terms on both sides of the sign must be satisfied to consider the statement as true), $U_L^{obs}(t)$ denotes the noise panel after passing the first step, and u_{body}^{obs} denotes the noise panel classified as containing a body-wave event. Note that we will also use the results of TWEED to generate features for an SVM classification, as will be described in the “Field-data application” section.

SYNTHETIC TEST

In this section, we present the application of TWEED to synthetic data. We investigate two different cases to highlight the relevance of

both steps in our method: (1) a surface transient source located 1000 m away from the array (case S1) and (2) a transient source located 1000 m below the center of the array (case S2). In both cases, the subsurface is homogeneous. Case S1 represents an ambient-noise source located at the surface and oriented in a direction perpendicular to the receiver lines. Because the source is at the surface and the model is homogeneous, the source mainly gives rise to surface waves because diving waves are not present. Thus, this model is used to test surface-wave detection. Case S2 represents a transient source that mimics an underground mine blast. Because the source is in the subsurface and the model is homogeneous, this source gives rise to relatively stronger body waves. Therefore, this case is used to test body-wave detection. In Figure 1c, we show the modeling setup with the two transient sources for which we perform the slowness discrimination. Figure 2 shows the results of TWEED — for case S1 in Figure 2a and for case S2 in Figure 2b. The green lines in the picture denote the range of scanned ray parameters (we choose values of ± 0.8 s/km to ensure that all expected surface waves are scanned). The red lines denote the predefined limits of expected slowness values for body waves (0.2 s/km); i.e., any

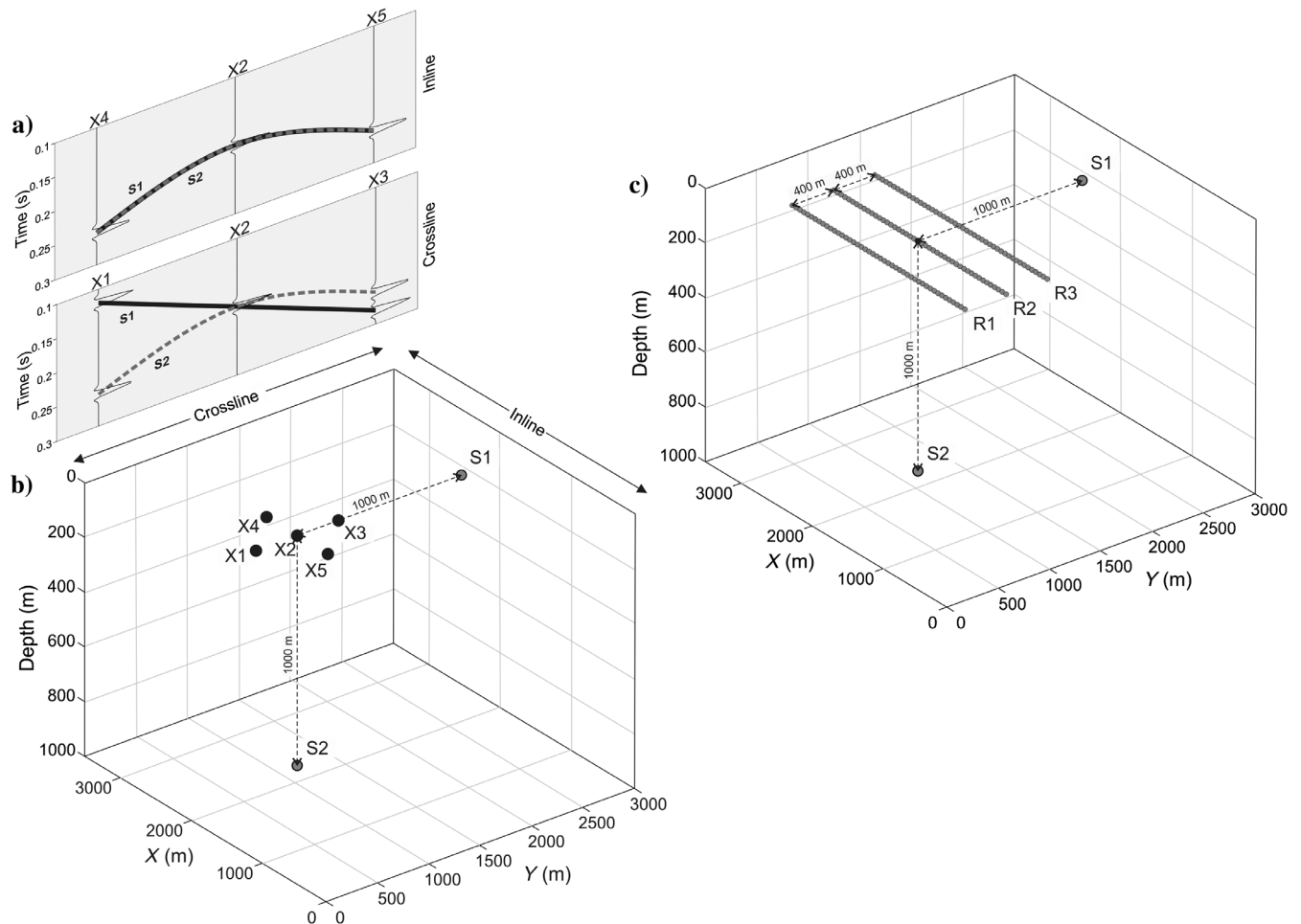


Figure 1. Sketch illustrating the basic concept behind TWEED. (a) Direct arrivals from sources S1 and S2 recorded at five receivers X1 to X5 forming a cross-shaped array. Analysis of arrivals recorded in the crossline direction allows for discrimination of the events from S1 and S2 as surface- and body-wave events, respectively. We can not discriminate between the events coming from source S1 and source S2, while analyzing their arrival times in the inline direction. Both sources are acting simultaneously, and we assume a constant propagation velocity of 5 km/s. (b) Configuration of the cross-shaped array formed by the five receivers. (c) Array formed by three receiver lines used to provide synthetic data for testing TWEED.

value falling inside this area is automatically accepted. The slope of the blue line indicates the value of the picked dominant ray parameter p_{MAX} . Note that discrimination between the two types of events — body and surface waves — is only possible because the wavefield is recorded at more than one receiver line. The summary of the illumination diagnosis performed for both cases is presented in Table 1. Because of the high apparent velocities picked in the virtual common-source panels, both models passed the first step. The discrimination between the two types of waves is possible only when we consider the arrival times of the analyzed events. As a result of the second step, energy traveling from below the array is distinguished from energy travelling along the surface.

Table 1. Results of TWEED for synthetic and field data. All values are given in km/s.

| Case S1 | | Case S2 | | Field example (scheduled mine blast) | | Field example (unscheduled mine event) | |
|---------------------|--------------------|------------------------|--------------------|--------------------------------------|--------------------|--|--------------------|
| Inline velocities | Crossline velocity | Inline velocities | Crossline velocity | Inline velocities | Crossline velocity | Inline velocities | Crossline velocity |
| 7.4; 6.3; 5.4 | <5 | 18.2; 16.2; 18.2 | >5 | 14.29; 11.11; 14.25 | >5 | 13.4; 10.11; 12.4 | >5 |

FIELD-DATA APPLICATION

In this section, we apply TWEED to ambient noise recorded by the Kylylahti array. The array was deployed in the vicinity of the Kylylahti polymetallic mine in Polvijärvi (Eastern Finland) as a part of the Cost-Effective Geophysical Imaging Techniques for Supporting Ongoing Mineral Exploration in Europe (COGITO-MIN) project. The COGITO-MIN project tackles in particular the cost aspects of mineral exploration by testing various novel seismic exploration technologies for high-resolution resource delineation (Koivisto et al., 2018). The Kylylahti array (Figure 3) consisted of 994 receiver stations distributed regularly over a 3.5 x 3 km area with 200 m line spacing and 50 m inline receiver spacing. Each receiver station was equipped with a bunched string of six 10 Hz vertical-component geophones and wireless data logger, recording noise at 2 ms for 20 h per day for 30 days, resulting in approximately 600 h of passive seismic data.

The survey area is located in the direct vicinity of the town of Polvijärvi town (population of >4000) providing abundant noise sources for the survey. Two fairly busy state roads cut through the whole survey area. The Kylylahti mining area is located to the northwest from a roundabout (Figure 3). Access to the mine is along gravel roads, used extensively by hauling trucks. The Kylylahti mine was active during the whole recording period. Routine mining activities included drilling (surface and underground), transporting ore and waste rock (surface and underground), scaling

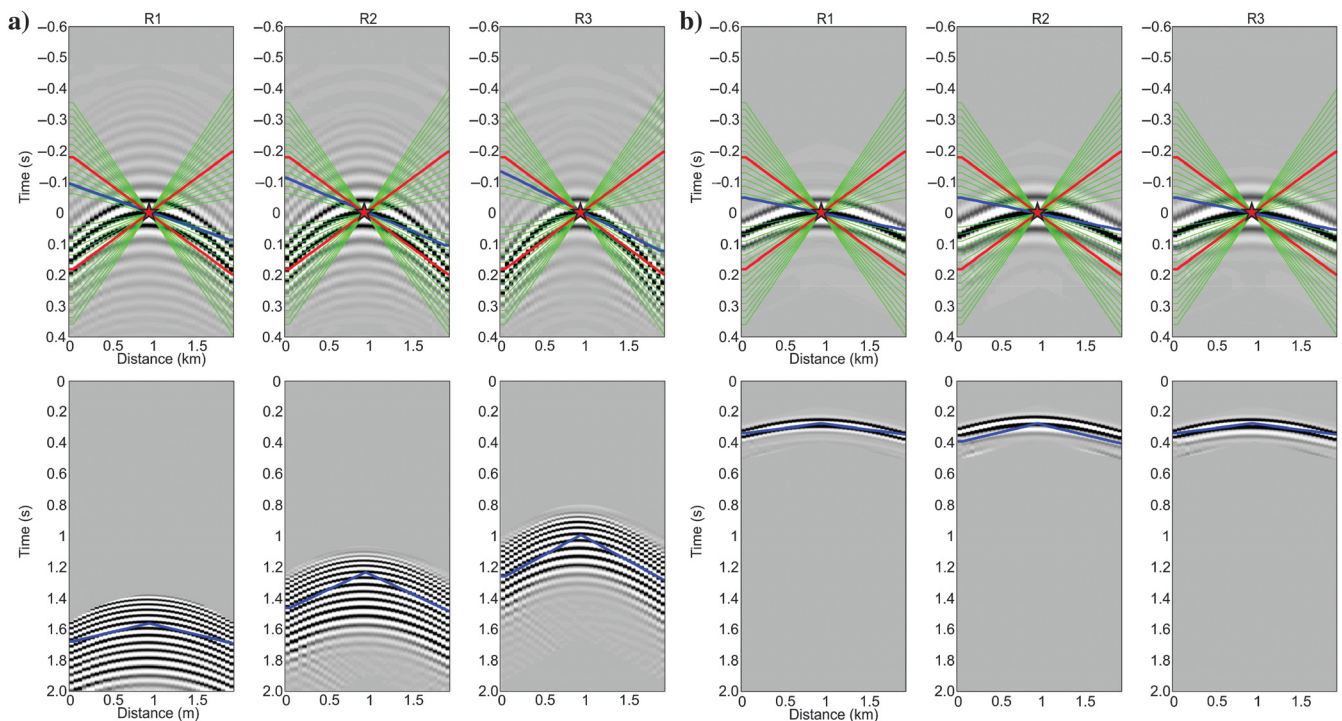


Figure 2. TWEED with synthetic data. Example TWEED evaluations for (a) a surface source (case S1) and (b) an underground source (case S2). Virtual common-source panels from the first step of TWEED (top row) are juxtaposed with the results of the second step (bottom row). The green lines indicate the range of scanned slownesses, the red lines are the predefined body-wave velocity limits, and the blue lines indicate the picked dominant slowness (evaluated in the first step) and the time of occurrence of the event (evaluated in the second step).

(underground), and mine ventilation (surface) among others. Other sources generating strong energy were the mine blasts, which occurred daily at depths ranging from a few hundred meters down to approximately 1000 m.

To test our detection algorithm, we first use only 1 h of noise recorded by the Kylylahti array. For this test, we select an hour during which a scheduled mine blast took place. We scan the data in 10 s long noise panels overlapping each other by 10%. We use mine blasts to benchmark our detection algorithm because they usually exhibit very high amplitudes and the times of their occurrence are approximately known. Figure 4 shows a mine blast that was de-

tected, and Figure 5 shows another body-wave event (not related to a mine blast) detected during the same hour. Figure 6a and 6b shows the results of applying TWEED to the mine blast and the body-wave event not related to the blasting, respectively. The body-wave event shown in Figure 5 exhibits lower amplitudes compared with the amplitudes of the mine blast (compare with Figure 4). Inspection of the correlated panels of the weaker event (Figure 6b, top row) indicates the low S/N of the dominant event because it is barely visible; however, by limiting the analysis to approximately $t = 0$ s, we can effectively determine the slowness of the dominant event. We suspect that this event is likely related to the routine mining activities. Table 1 summarizes the evaluated apparent velocities for the two events. Overall, for this hour-long noise panel, we detect seven different body-wave events.

In the next step, we run our method on the full data set, i.e., 600 h of recordings. The resulting time distribution of the detected events is presented in Figure 7. Figure 7a presents the average distribution of noise sources per hour during one day, and Figure 7b shows the number of detected events for each day. Both graphs indicate persistent presence of body-wave events during the whole recording period. The high activity of noise sources at 5 pm local time (see Figure 7a) is related to the scheduled mine shooting and the high activity in the evening (5–12 pm) is related to mine cleaning after the blast. The lower number of detected events in periods when an active seismic survey was done (denoted with the gray bars) is due to the fact that at those times, underground in-mine vertical seismic profiling shots were not performed, to avoid interference with the controlled surface shots, whereas such in-mine shots were performed outside those times. The distribution of body-wave events during the one month of recording (see Figure 7b) shows the presence of noise sources for each day of the recording with some days exhibiting higher numbers of detected body-wave events. For the whole recording period, we detect 1093 events.

SVM applied to the field data

Above, we show the results of detecting body-wave events using TWEED. We demonstrate with the synthetic example that the second step of the method is necessary to distinguish body-wave events from surface waves. The question we pose here is whether we can omit the second (computationally costly!) step and still obtain reasonable detections. Toward answering this question, we use an SVM algorithm in a binary seismic-event classification problem (body-wave versus non-body-wave event). SVM is a supervised machine-learning method based on statistical learning theory (Vapnik, 1998). The key idea in this method is to find the line (hyperplane) that splits (i.e., classifies) the input-variable space. This hyperplane is learned from training data using an optimization procedure that maximizes the distance margin between the line and the closest data points. The general procedure is as follows: (1) First, SVM maps the input data into the

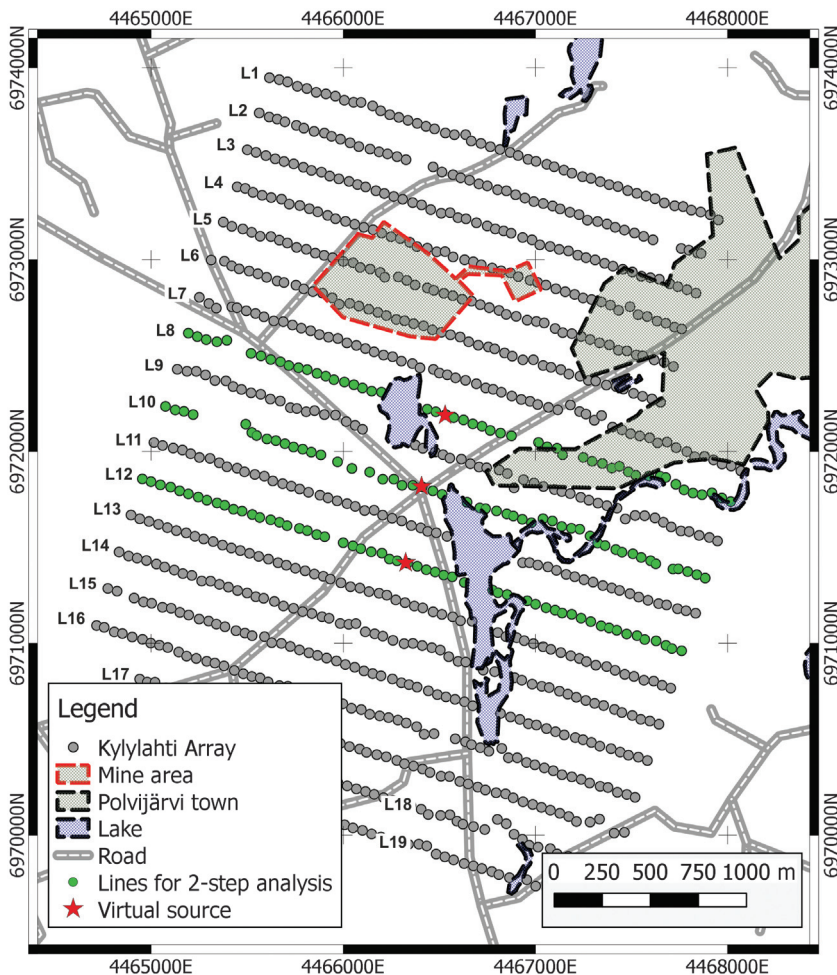


Figure 3. Layout of the Kylylahti array. The receiver lines used in the study are shown in green.

Table 2. Cross-validation results.

| | Average accuracy | | Standard deviation | |
|--------------|------------------|----------|--------------------|----------|
| | Training set | Test set | Training set | Test set |
| Small subset | 0.963 | 0.962 | 0.026000 | 0.058324 |
| Whole data | 0.997 | 0.997 | 0.000239 | 0.000680 |

high-dimensional subspace using a nonlinear mapping chosen a priori. The mapping process is performed using a set of functions, known as kernels. (2) Then, the hyperplane is selected to best separate the points in the input-variable space by their class. (3) Finally, the prediction about class for yet-unclassified data is made based on which side of the gap dictated by the hyperplane the data fall into.

Here, we use SVM to classify the input noise panels based on their illumination characteristics into either containing a body-wave event or not. As the input features, we select the dominant ray parameter of the event passing through time zero at the position of the virtual source in a virtual common-source panel ($p_{\text{MAX}} = \max(\hat{C}_L^s(x_A, \mathbf{p}))$) and the mean value of the three ray parameters characterized by the three highest values of the slant-stack-transformed virtual common-source panel evaluated at $t = 0$ s ($\bar{p}_{\text{MAX}} = \frac{1}{3} \sum_{i=1}^3 p_{\text{MAX}i}$), where $p_{\text{MAX}i}$ denotes the i th highest value of the picked ray parameter. We choose these values because they are obtained from the first step of our illumination-diagnosis method.

Because the whole data set has already been scanned with TWEED, we have data ready to be used in SVM. We first evaluate the performance of SVM on a small subset of the data and test it on the same hour of noise that served as the benchmark for TWEED in the previous section. As mentioned before, we perform noise scanning with TWEED in 10 s long windows with 10% overlap; therefore, 1 h of recorded seismic noise provides 399 separate noise panels as the input for SVM. We split the data into training and test sets with the ratio of 0.8, and, as the kernel function, we select the Gaussian function (Smola and Schölkopf, 2004). To focus on the influence of parameters derived from the seismic data, the other settings are set to values suggested in Pedregosa et al. (2011). Figure 8 shows the results of applying SVM to the ambient-noise recordings from the Kylylahti array. We compare the SVM classification against the result from TWEED, or in other words, we use the latter as the ground truth. Thus, we cannot outperform the result from TWEED in the number of picked body-wave events, but we aim to shorten the time for the second step in TWEED by exchanging it for SVM.

The results show that, in general, the model is able to distinguish (see Figure 8a) and predict (see Figure 8b) between the two classes of seismic noise panels when provided with their basic slowness characteristics — we observe clearly visible binary clustering. The small overlap between the gray and black points (some gray points fall into the black area and vice versa) could be attributed to the fact that surface sources at relatively far distances in the crossline direction can be recorded as events with high apparent velocity (see Figures 1a and 2a). Note that values displayed in this graph are subjected to feature scaling, which is a conventional step in SVM

data preprocessing (Pedregosa et al., 2011). To describe our results more quantitatively, we show the confusion matrices (see Figure 9). Confusion matrices show the number of correct and incorrect predictions from a machine-learning model. When the model predicts the actual class, the sample is listed on the diagonal of the confusion matrix. When the model predicts the wrong class, the sample is listed off the diagonal. From the training-set confusion matrices presented in Figure 9, we see that from the total of 319 noise recordings, SVM was able to correctly predict 303 non-body-wave events and five out of the seven body-wave events.

A representative example of an incorrect detection obtained with SVM is presented in Figure 10. It exhibits a high-amplitude

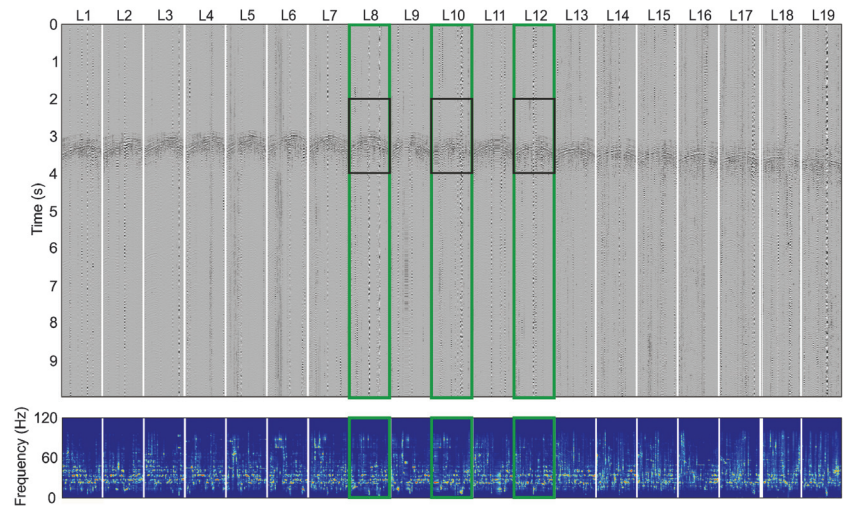


Figure 4. Scheduled mine event (underground blast) detected with TWEED (as a body-wave event). The detected event, recorded by 19 receiver lines, is shown at the top, and the relevant power spectral density is plotted at the bottom. The green rectangles mark the receiver lines selected for TWEED. The black rectangles mark the part of the detected event shown in the bottom row in Figure 6a.

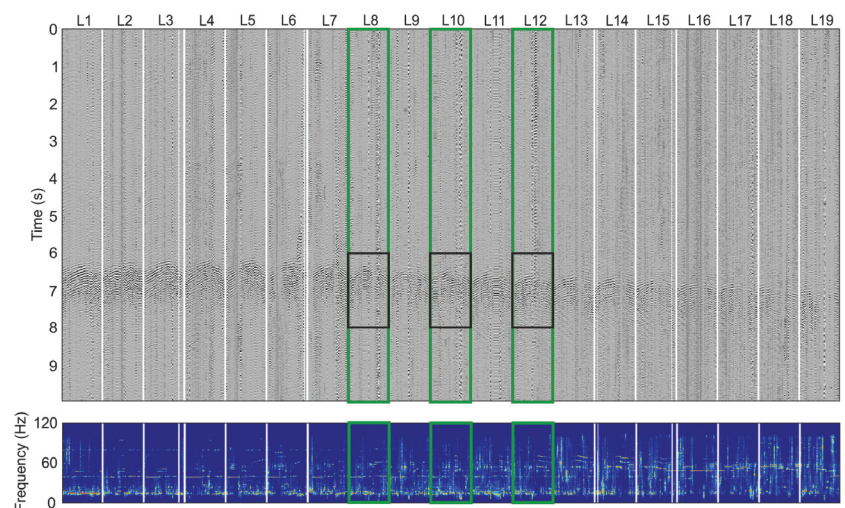


Figure 5. Event likely related to underground mine activity (other than mine blasts) detected with TWEED (as a body-wave event). The detected event recorded by 19 receiver lines is shown at the top, and the relevant power spectral density is plotted at the bottom. The green rectangles mark the receiver lines selected for TWEED. The black rectangles mark the part of the detected event shown in the bottom row in Figure 6b.

surface-wave event originating in the vicinity of the receiver lines selected for TWEED. This event manifests itself as sequence of hyperbolic wavefronts likely related to road traffic. The reason for its detection is explained by the modeling results shown in Figures 1a and 2a. We feed the SVM with slowness parameters obtained from the first step of TWEED. For the event presented in Figure 10, the

apparent velocities evaluated in the correlated panel are relatively high (>5 km/s) and are thus similar to the P-wave velocity. As we see in the inset of Figure 10, a package of hyperbola apexes for this event arrives with a delay from one of the lines selected for TWEED to another. Based on the value of this delay, the evaluation of the second step of TWEED allows us to label this event as a surface-wave event.

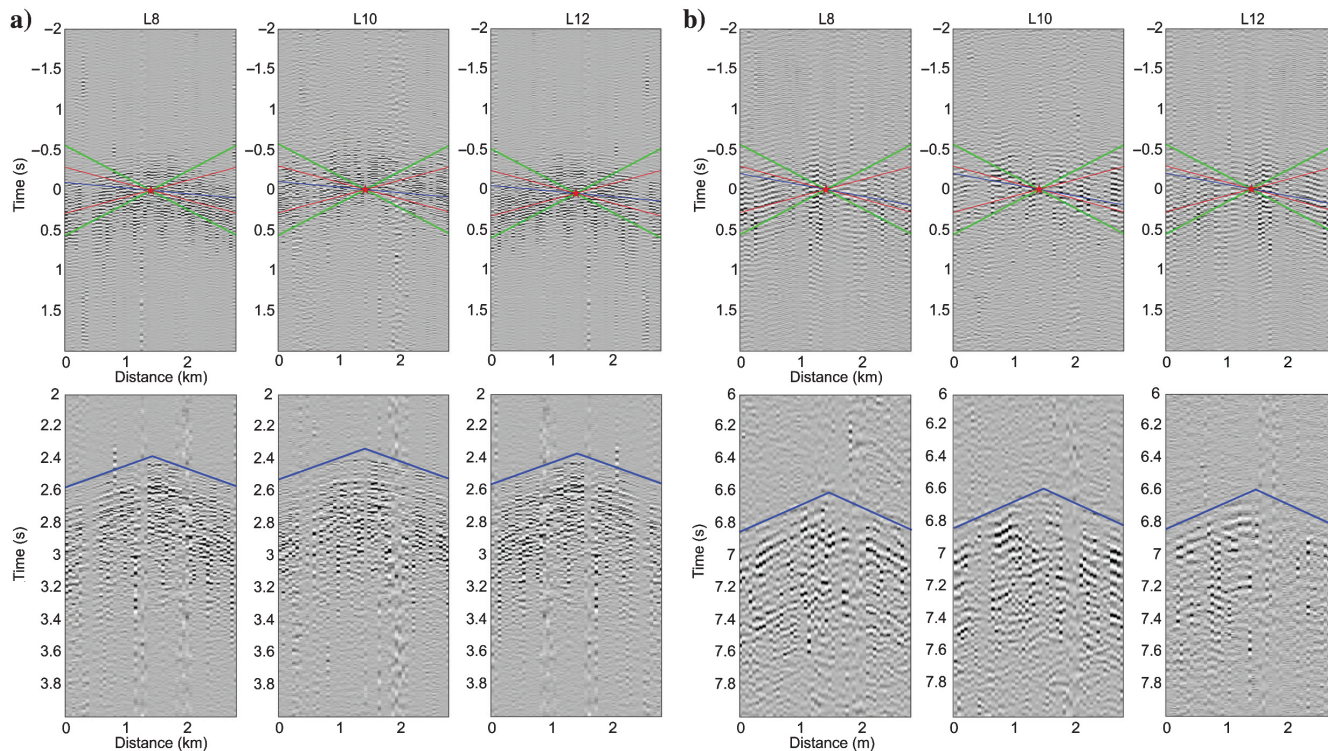


Figure 6. Performance of TWEED for the two events related to underground mine activity: (a) scheduled mine blast shown in Figure 4 and (b) possibly routine mining activity shown in Figure 5. The result of TWEED is presented in the same manner as in Figure 2.

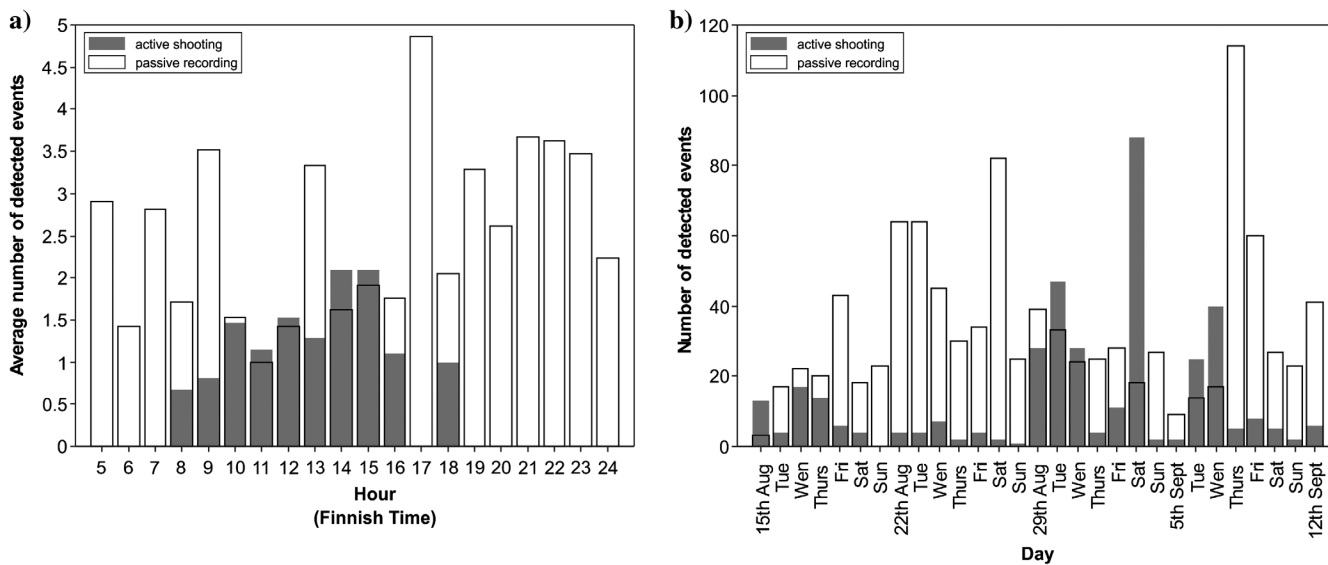


Figure 7. Time distribution of body-wave events detected with TWEED. (a) The average number of detected events per hour during a recording day. (b) The number of detected events for each day of recording. The gray bars indicate periods when active-source shooting also took place at the surface, and the lighter color denotes the passive recordings. Local time is used.

We use the results derived from the whole recording period (600 h of ambient-noise recordings) to evaluate the performance of SVM with a bigger training set. Before applying SVM, we preprocess the data by removing ray parameters with values of zero as well as values that are too high (equal to the high-end limits of the scanning range). Figure 8c and 8d shows the 2D plots for the training and test sets. In general, we can see that SVM is able to distinguish between the two groups of events — body waves and surface waves. The clustering shape visible in the results obtained for the hour-long data is sustained. Note that we again compare the SVM results against the result from TWEED.

The evaluation of the SVM model accuracy depends on the choice of the test set; therefore, it is not very relevant to judge the model performance on only one test. To overcome this problem, a cross-validation test is usually performed. In this approach, we split the training set into k folds (the default value is 10). We train our model on nine folds and test it on the remaining fold. As a result, we can train our model on 10 different combinations of training and test sets, which provides us 10 different model accuracies. The mean value of these 10 accuracies and its standard deviation for the

SVM performance tested with the two sets of data is presented in Table 2.

The detection results obtained from TWEED were visually inspected for their correctness, which justifies our use of them as a ground truth in this study. As we write above, SVM provided with labels obtained from the first step of TWEED cannot outperform the full two-step TWEED in the detection of body-wave events. Figure 8 shows the results obtained with SVM using two input features, which were effectively the slowness parameters averaged over three recording lines. Instead of averaging, the input features can be obtained from each line separately, effectively providing two slowness parameters for each line, i.e., six input features instead of two. To investigate how the behavior of SVM could be influenced by another selection of input features, we test the SVM using various combinations of those six values. We find that the best detection rate can be achieved using four input features, namely, \tilde{p}_{MAX} for each recording line and the p_{MAX} for the central receiver line. Confusion matrices for SVM provided with those features (Figure 11) indicate that by careful selection of input features the detection accuracy of body wave events is improved by approximately 13%.

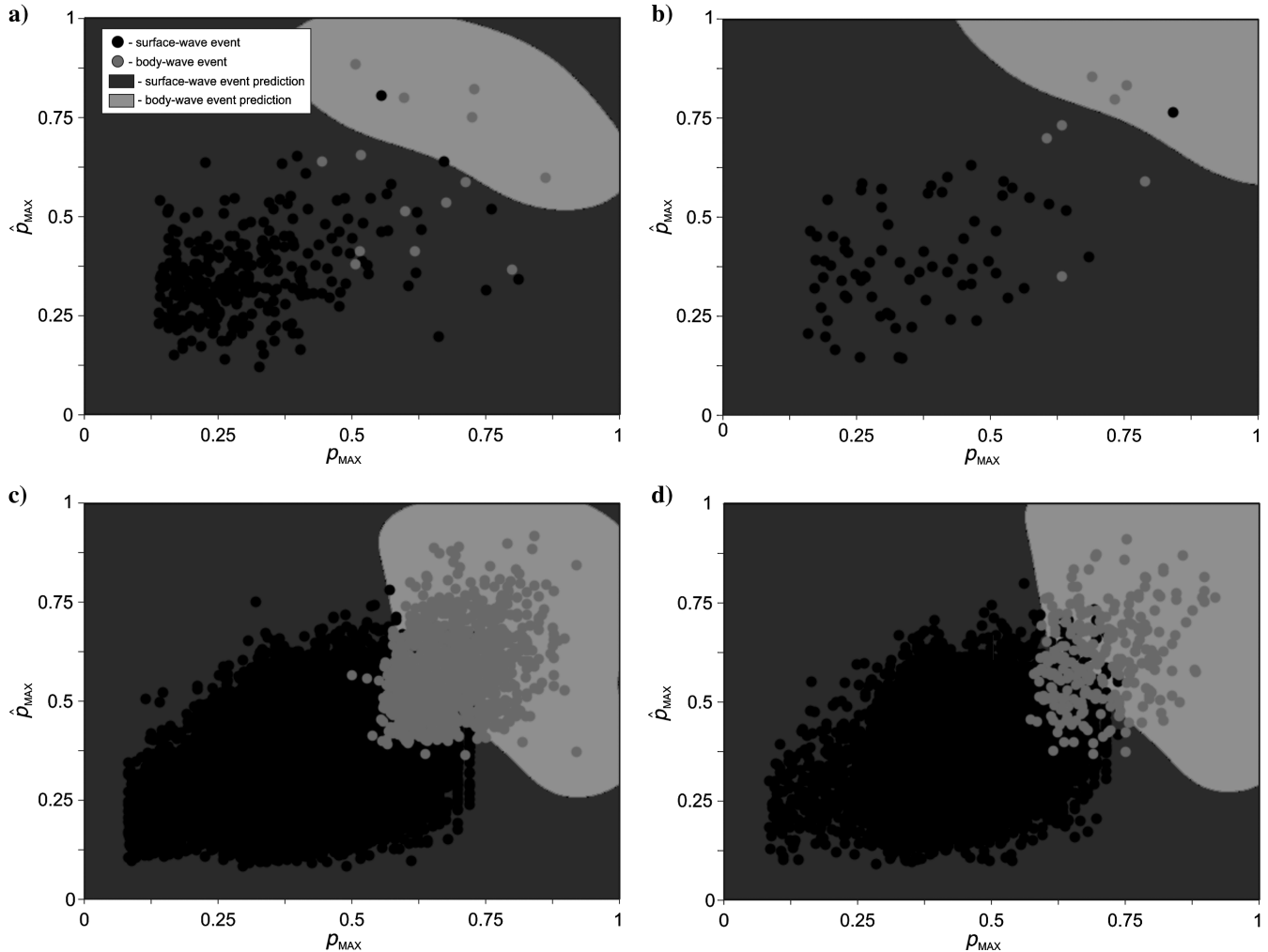


Figure 8. Performance of the SVM in detection of body-wave events using input features derived from the first step of TWEED. Two examples are shown: (a and b) for 1 h of ambient-noise recordings and (c and d) using the whole recorded data set. For both cases, the SVM performance is shown for the (a and c) training set and (b and d) the test set. For display purposes, the values for both axes are normalized. The color of the dots indicates results obtained from TWEED, and the shaded regions are the results determined by the SVM.

Computational cost of TWEED and SVM

The actual computational time depends on the working environment, i.e., computational resources. Therefore, in this study, we compare the computational time of TWEED and SVM using relative values. Running TWEED on the whole data set (600 h of ambient noise recorded by approximately 1000 receivers) takes approximately 150% the time of the hybrid approach combining the first step of TWEED and SVM with two input features. We consider SVM with two input features as a compromise between the accuracy and speed. The hybrid approach with the first step of TWEED followed by SVM with four input features (striving for a higher detection accuracy compared with just two input features) takes 70% of the time needed for running TWEED on the whole data set. Please note that the above

values are subjective numbers and might be specific for this study. In general, the important factors influencing any detection study using the methodology described above would be the (1) computing resources, (2) ratio of data distribution between TWEED and SVM, and (3) number of input features. These factors will likely vary for one case study to another. We argue that using four input features should be a reasonable choice for an initial run because the relatively small increase in computational cost (compared with two input features) provides increased accuracy.

DISCUSSION

In this study, we show the results of detecting body-wave events based on their slowness characteristics. Seismic-event detection naturally forms a binary classification problem. We

approach this using two methods: an automated thresholding method (TWEED) and SVM. Using TWEED, we are able to effectively scan our data and detect approximately 1000 events distributed more than 600 h of ambient-noise recordings from the array of approximately 1000 sensors. Our method is robust because it requires very limited previous knowledge — just the lowest velocities of presumed body-wave events in the recording area need to be known. Second, it can be easily adapted to other types of events by adjusting the predefined slowness thresholds. By adjusting the range of the scanned ray parameters and arrival-time differences of the target events, TWEED can be used for detecting noise sources located in areas providing optimal illumination, which could be important for selective stacking used in passive SI imaging.

The robustness is also related to applying the simplest form of stacking, which is linear. Even though we use this simplest form of slowness-illumination diagnosis (linear slant-stack), more sophisticated algorithms can be easily implemented (e.g., hyperbolic, parabolic, etc.). In fact, any type of coherent signal considered to be a seismic event could be scanned for by measuring its similarity to the specified pattern.

TWEED showed its effectiveness in detecting the strong body-wave events such as mine blasts and the weaker body-wave events related to other underground mining activities. As a result of analyzing the virtual common-source panels in the first step of TWEED, the detection is limited to the strongest transient source acting in a given short time period. For detecting weaker sources, the raw noise recordings should be subjected to simple amplitude normalization (e.g., trace balancing; Draganov et al., 2007) together with band-pass filtering to enhance the desired type of an event (Draganov et al., 2009; Quiros et al., 2016).

Our method can be used for a variety of different acquisition geometries, provided that at least two receiver lines (or approximations of lines) with sufficiently dense (to avoid aliasing) inline sampling are available. However, the key requirement

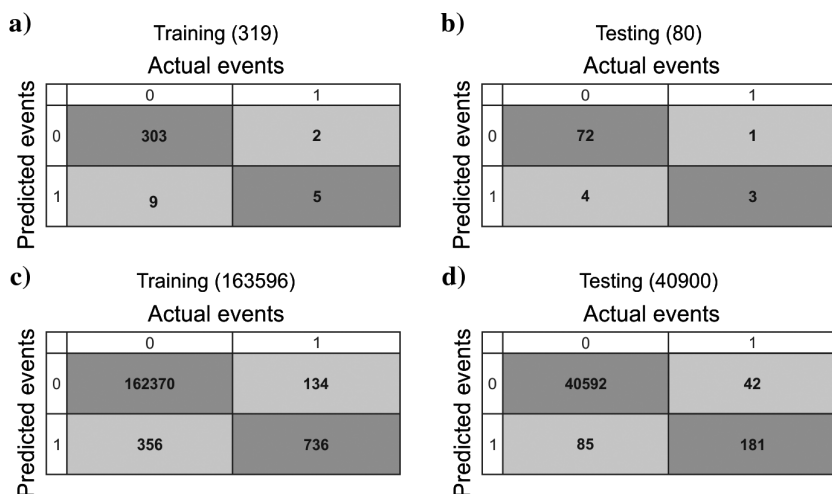


Figure 9. Confusion matrices for the results presented in Figure 8 for (a and c) the training set and (b and d) the test set. The diagonal numbers (darker colors) denote the number of correct predictions, whereas incorrect predictions are listed off diagonal (lighter colors). Values in brackets denote the total number of events in a given subset. Numbers 0 and 1 denote surface-wave and body-wave events, respectively.

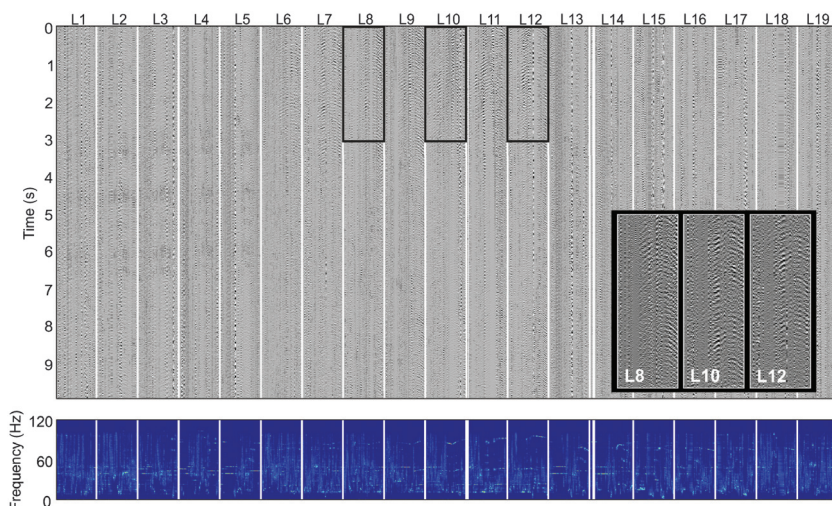


Figure 10. Event incorrectly detected by SVM. The detected event recorded by 19 receiver lines is shown at the top, and the relevant power spectral density is plotted at the bottom. The inset shows the magnified parts along the three receiver lines selected for TWEED and are indicated with black rectangles.

for TWEED depends on the ambient-noise wavefield in the area; i.e., the energy of the seismic events present in the recording area should be sufficiently high to be recorded by a few separate receiver lines.

One of our primary goals was to develop a real-time data-scanning tool. Imaging body-wave reflections using SI requires body-wave events present in the noise recordings (Draganov et al., 2013). Therefore, having an idea of the body-wave content in our recordings would constitute an effective quality-control tool for ambient-noise SI, which can be used, e.g., to determine for how long a given array should be deployed. For such an application, the computation time becomes a crucial parameter. Even though TWEED is effective, in some cases of clear body-wave arrivals evaluating both steps might not be desirable due to required computation times. We apply an SVM technique to investigate the possibility of bypassing the second step in our method, and thus we obtain a more time-efficient method. In most cases, slowness values derived only from correlated panels contain sufficient information to recognize body-wave events using SVM. The results shown for the 1 h long panel indicate that in fact the number of input data does not have to be large.

As shown in many field experiments, surface measurements in areas with human activity are usually dominated by near-surface sources (Draganov et al., 2013; Cheraghi et al., 2015; Nakata et al., 2015). This means that usually the number of body-wave events is small compared with the surface-wave activity. In our case, we observe good performance of SVM providing only seven body-wave events and 392 surface-wave panels. This test proves its feasibility for ambient-noise measurements done at the surface. It also shows that compared with TWEED, the SVM approach is more biased by the surface-wave content of the recorded ambient-noise wavefield. The results of SVM for the whole data set do not dramatically affect the prediction accuracy, so we argue that captured body-wave events manifest themselves with similar ray-parameter characteristics during the whole recording period. The relatively high detection rate for SVM suggests that the choice of input parameters was adequate. On the other hand, the overlapping pattern visible in Figure 8c suggests that the SVM performance could be further increased. Changing the input features, adjustment of hyperparameters, and multidimensional scaling with additional input features are potential solutions for improving the SVM performance. Our primary objective in applying SVM is to remove the need for the second step in TWEED; therefore, the choice of input features was limited to ray parameters derived exclusively from the first step. Although the dominant ray parameter is a natural choice, the average of the three highest parameters is somewhat experimental in terms of choice. Its effectiveness might be related to the fact that the mine activities generate body-wave events, which reach our array in the form of several wavefronts appearing as several strong events around time zero in the correlated panels. The lower number of detected body-wave events in comparison with TWEED might be acceptable when real-time detection for very long recordings with lower computational costs is desirable.

The virtual common-shot panels in TWEED are derived from correlating the central trace

of a given noise panel with the complete panel. The user-dependent parameters in TWEED are the (1) locations of receiver lines selected for analysis, (2) number of those lines, and (3) location of the master trace. If the central receiver is a dead trace or exhibits a poor S/N, the adjacent receiver could be chosen as a virtual source as well. We recommend selecting a subset of lines that is representative for the whole recording array. By this, we mean that events recorded by the central lines of the array are more likely to be recorded by the whole array than events recorded by peripheral lines chosen only from one side of the array. The number of the chosen receiver lines significantly increases the computational cost of the automatic detection; therefore, it should be kept as low as possible while guaranteeing the highest number of correct detections and minimizing the false ones. For the Kylylahti array, by means of a trial-and-error approach combined with visual inspection of detected panels, we find that three lines is the optimal choice balancing the computational effort and the accuracy of detections. The computational efficiency could further be increased if the number of receivers per line is reduced. This could be done if an initial number of detected events shows that the illumination angles and frequencies of the dominant body-wave events allow inline receiver decimation (e.g., taking every second receiver). Such a choice, though, might lead to aliasing of the recorded surface-wave noise. Thus, opting for an inline receiver decimation should be done after careful evaluation of the risks of aliased surface waves against the gains in computation.

In our illumination diagnosis, we rely on the ray parameters of events in the noise panels. In general, the range of the values seen for the field data can be explained by a source placed 1000 m below the center of the recording array, as shown using the synthetic data. Lower ray-parameter values for the field data suggest that sources captured by the Kylylahti array are distributed at shallower depths (<1000 m). The values of the dominant ray parameters evaluated in the first step of the illumination diagnosis would increase with the increasing depth of a given transient source. Furthermore, if the

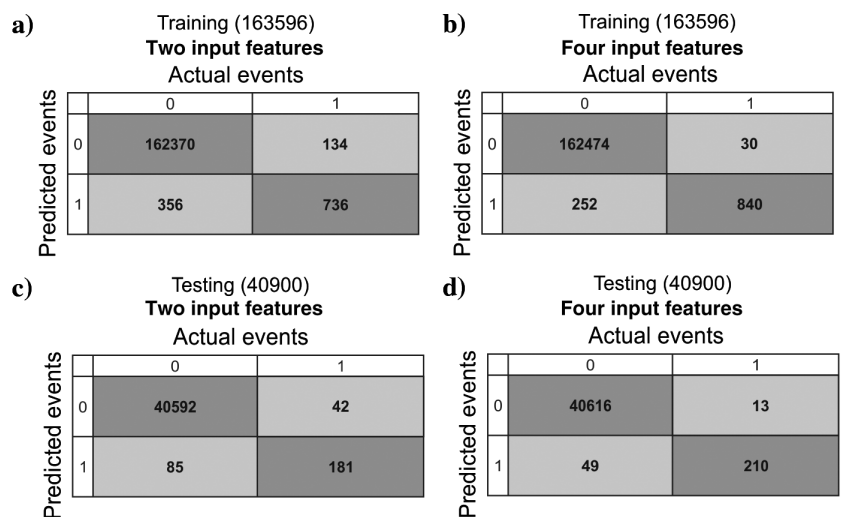


Figure 11. Confusion matrices for the SVM results obtained with (a and c) two and (b and d) four input features. The diagonal numbers (darker colors) denote the number of correct predictions, whereas incorrect predictions are listed off diagonal (lighter colors). For both cases, the SVM performance is shown for (a and b) the training set and (c and d) the test set. Values in brackets denote the total number of events in a given subset. Numbers 0 and 1 denote the surface- and body-wave events, respectively.

location of a source acting in a given panel deviates from the center of the receiver array, this will be detected via a shift in the minimum value of the picked ray parameter from the middle receiver line to the peripheral lines taken for analysis. Incorporating this knowledge would allow TWEED to also be used for favoring noise sources located in the desired stationary-phase areas (Forghani and Snieder, 2010) and, consequently, using it as a robust selective-stacking technique commonly used in passive SI processing (Draganov et al., 2013; Nakata et al., 2015; Olivier et al., 2015).

In this study, by using just two simple parameters, we are able to discriminate between two basic types of seismic events (body wave or not). However, our method can be modified to scan for ambient-noise events of more complex characteristics. It seems viable to be able to provide a more precise description of the ambient-noise wavefields by decomposing them into several classes of seismic events by using clustering machine-learning techniques or neural networks, e.g., convolutional neural networks (CNNs). In general, if we expect the passive array to be illuminated from several main directions during its recording time, e.g., a mine, a crusher, a power plant, a nearby town, a main road, etc., SVM could be the method of choice. If we do not have a priori expectations about the main illumination directions of the passive arrays, e.g., an area with little or continuously changing anthropogenic noise, we should consider other machine-learning techniques. SVM provides relatively good results with a small number of input features, so the target seismic waves must be distinguishable by some fundamental feature (such as the ray parameter in this study). In areas with more complex ambient seismic noise, random noise of unknown nature might hinder describing coherent seismic events using mathematical expressions. Thus, it would be more difficult to choose one feature by which we could discriminate between types of waves. Therefore, techniques benefiting from not-obvious relations between different input features should be considered. A good example of such techniques is CNNs, which are capable of distinguishing complex shapes in 2D images (Krizhevsky et al., 2012). Inspired by the results presented in this study, we recommend two different approaches for binary seismic-event detection on large volumes of ambient-noise data: (1) application of TWEED for thorough and precise information and extraction of body-wave events and (2) a hybrid approach combining the application of the full TWEED only to a small subset of the data (e.g., a few hours of noise) and then the consecutive application of the SVM model, trained with this small subset, to the whole (remaining or coming from real-time recording) data set. SVM uses ray parameters derived only from virtual common-shot panels (i.e., from the first step of TWEED). This approach can be used for a fast QC of recordings to provide general metrics about the body-wave content or for real-time evaluation of very large and long data sets, rather than extracting every single event.

CONCLUSION

We investigated the feasibility of an automatic illumination-diagnosis method and a machine-learning approach for binary detection of body-wave events in ambient seismic noise recorded by large-number receiver arrays. For this purpose, we developed TWEED, which is an extension of an illumination-diagnosis method introduced previously for crossing lines to 3D seismic surveys with noncrossing lines. We evaluated the illumination characteristics of noise panels by simultaneous analysis along several receiver lines. Because of these characteristics, our method becomes an efficient

detection tool when geophone arrays with sparse crossline sampling are used (as in conventional 3D seismic surveys). Using synthetic data, we demonstrated that our method is able to discriminate between two basic seismic event types (body-wave versus surface-wave events). We validated our method with approximately 600 h of ambient-noise data recorded by a approximately 1000 receiver array deployed over an active underground Kylylahti mine in Eastern Finland. We showed that our method is efficient in detecting evident seismic events such as mine blasts, but also weaker events related to routine underground mining activities.

We also investigated the possibility of decreasing the computational costs required for detecting body-wave events by using a SVM technique, using as the input feature slowness parameters derived from the analysis of correlated noise panels. In this way, we effectively limited the analysis to just the first step of TWEED followed by the SVM classification. The SVM method performed well and correctly predicted most of the seismic events (body and surface waves) in the field data. The good performance achieved with relatively few input features suggests that combining the SVM approach with TWEED might be a time-efficient solution because just 1 h of the approximately 600 h of ambient-noise recordings was analyzed before prediction.

ACKNOWLEDGMENTS

COGITO-MIN has been funded through ERA-MIN, which is a network of European organizations owning and/or managing research programs on raw materials. The funding for the Finnish COGITO-MIN project partners comes from TEKES and for the Polish project partners from the NCBR. M. Chamarczuk's visit at TU Delft was funded by the statutory activities of the IG PAS (project number: 500-10-40). We thank the field crews from the University of Helsinki, Geological Survey of Finland, IG PAS, and Boliden for deploying the Kylylahti array. We thank NovaSeis field personnel for troubleshooting the array and data handling. We thank J. Etgen and anonymous reviewers for useful suggestions and comments. All calculations and analyses regarding SVM were implemented in Python using the freely available Scikit-learn package (Pedregosa et al., 2011).

REFERENCES

- Allen, R., 1978, Automatic earthquake recognition and timing from single traces: *Bulletin of the Seismological Society of America*, **68**, 1521–1532.
- Almagro Vidal, C., D. Draganov, J. van der Neut, G. Drijkoningen, and K. Wapenaar, 2014, Retrieval of reflections from ambient noise using illumination diagnosis: *Geophysical Journal International*, **198**, 1572–1584, doi: [10.1093/gji/ggu164](https://doi.org/10.1093/gji/ggu164).
- Bensen, G. D., M. H. Ritzwoller, M. P. Barmin, A. L. Levshin, F. Lin, M. P. Moschetti, N. M. Shapiro, and Y. Yang, 2007, Processing seismic ambient noise data to obtain reliable broad-band surface wave dispersion measurements: *Geophysical Journal International*, **169**, 1239–1260, doi: [10.1111/j.1365-246X.2007.03374.x](https://doi.org/10.1111/j.1365-246X.2007.03374.x).
- Ben-Zion, Y., F. L. Vernon, Y. Ozakin, D. Zigone, Z. E. Ross, H. Meng, M. White, J. Reyes, D. Hollis, and M. Barklage, 2015, Basic data features and results from a spatially dense seismic array on the San Jacinto fault zone: *Geophysical Journal International*, **202**, 370–380, doi: [10.1093/gji/ggv193](https://doi.org/10.1093/gji/ggv193).
- Bormann, P., 1998, Conversion and comparability of data presentations on seismic background noise: *Journal of Seismology*, **2**, 37–45, doi: [10.1023/A:1009780205669](https://doi.org/10.1023/A:1009780205669).
- Brenguier, F., P. Kowalski, N. Ackerley, N. Nakata, P. Boué, M. Campillo, E. Larose, S. Rambaud, C. Pequegnat, T. Lecocq, P. Roux, V. Ferrazzini, N. Villeneuve, N. M. Shapiro, and J. Chaput, 2016, Toward 4D noise-based seismic probing of volcanoes: Perspectives from a large-N experiment on Piton de la Fournaise Volcano: *Seismological Research Letters*, **87**, 15–25, doi: [10.1785/0220150173](https://doi.org/10.1785/0220150173).

- Cercione, J. A., 1993, Fuzzy logic classification of seismic events: 25th Southeastern Symposium on System Theory, 388–391, doi: [10.1109/SSST.1993.522808](https://doi.org/10.1109/SSST.1993.522808).
- Chaouch, A., and J. L. Mari, 2006, 3-D land seismic surveys: Definition of geophysical parameters: Oil and Gas Science and Technology-Rev. IFP, **61**, 611–630, doi: [10.2516/ogst.2006002](https://doi.org/10.2516/ogst.2006002).
- Chapman, H., 1981, Generalized Radon transforms and slant stack: Geophysical Journal International, **66**, 445–453, doi: [10.1111/j.1365-246X.1981.tb05966.x](https://doi.org/10.1111/j.1365-246X.1981.tb05966.x).
- Cheraghi, S., J. A. Craven, and G. Bellefleur, 2015, Feasibility of virtual source reflection seismology using interferometry for mineral exploration: A test study in the Lalor Lake volcanogenic massive sulphide mining area, Manitoba, Canada: Geophysical Prospecting, **63**, 833–848, doi: [10.1002/2015JB011870](https://doi.org/10.1002/2015JB011870).
- Cheraghi, S., J. White, D. Draganov, G. Bellefleur, J. A. Craven, and B. Roberts, 2017, Passive seismic reflection interferometry: A case study from the Aquistore CO2 storage site, Saskatchewan, Canada: Geophysics, **82**, no. 3, B79–B93, doi: [10.1190/GEO2016-0370.1](https://doi.org/10.1190/GEO2016-0370.1).
- Corciulo, M., P. Roux, M. Campillo, D. Dubucq, and W. A. Kuperman, 2012, Multiscale matched-field processing for noise-source localization in exploration geophysics: Geophysics, **77**, no. 5, KS33–KS41, doi: [10.1190/geo2011-0438.1](https://doi.org/10.1190/geo2011-0438.1).
- Dales, P., P. Audet, G. Olivier, and J. P. Mercier, 2017, Interferometric methods for spatio-temporal seismic monitoring in underground mines: Geophysical Journal International, **210**, 731–742, doi: [10.1093/gji/ggx189](https://doi.org/10.1093/gji/ggx189).
- Draganov, D., X. Campman, J. W. Thorbecke, A. Verdel, and K. Wapenaar, 2009, Reflection images from ambient seismic noise: Geophysics, **74**, no. 5, A63–A67, doi: [10.1190/1.3193529](https://doi.org/10.1190/1.3193529).
- Draganov, D., X. Campman, J. W. Thorbecke, A. Verdel, and K. Wapenaar, 2013, Seismic exploration-scale velocities and structure from ambient seismic noise (>1Hz): Journal of Geophysical Research: Solid Earth, **118**, 4345–4360, doi: [10.1002/jgrb.50339](https://doi.org/10.1002/jgrb.50339).
- Draganov, D., K. Wapenaar, W. Mulder, J. Singer, and A. Verdel, 2007, Retrieval of reflections from seismic background-noise measurements: Geophysical Research Letters, **34**, L04305, doi: [10.1029/2006GL028735](https://doi.org/10.1029/2006GL028735).
- Draganov, D. S., and E. Ruigrok, 2015, Passive seismic interferometry for subsurface imaging, in M. Beer, E. Patelli, I. Kougioumtzoglou, and I. Siu-Kui Au, eds., Encyclopedia of earthquake engineering: Springer, 1–13.
- Forghani, S., and R. Snieder, 2010, Underestimation of body waves and feasibility of surface-wave reconstruction by seismic interferometry: The Leading Edge, **29**, 790–794, doi: [10.1190/1.3462779](https://doi.org/10.1190/1.3462779).
- Freed, D., 2008, Cable-free nodes: The next generation land seismic system: The Leading Edge, **27**, 878–881, doi: [10.1190/1.2954027](https://doi.org/10.1190/1.2954027).
- Gray, H. S., 2013, Spatial sampling, migration aliasing, and migrated amplitudes: Geophysics, **78**, no. 3, S157–S164, doi: [10.1190/geo2012-0451.1](https://doi.org/10.1190/geo2012-0451.1).
- Hansen, S. M., and B. Schmandt, 2015, Automated detection and location of microseismicity at Mount St. Helens with a large-N geophone array: Geophysical Research Letters, **42**, 7390–7397, doi: [10.1002/2015GL064848](https://doi.org/10.1002/2015GL064848).
- Johnson, D. H., and D. E. Dudgeon, 1993, Array signal processing: Concepts and techniques: Prentice Hall.
- Jousset, P., H. Blanck, S. Franke, M. Metz, K. Ágústsson, A. Verdel, T. Ryberg, G. Páll Hersir, C. Weemstra, D. Bruhn, and Ó. Flovenz, 2016, Seismic tomography in Reykjanes, SW Iceland: Presented at the European Geothermal Congress.
- Kao, H., and S. J. Shan, 2004, The source-scanning algorithm: Mapping the distribution of seismic sources in time and space: Geophysical Journal International, **157**, 589–594, doi: [10.1111/j.1365-246X.2004.02276.x](https://doi.org/10.1111/j.1365-246X.2004.02276.x).
- Koivisto, E., M. Malinowski, S. Heinonen, C. Cosma, M. Wojdyla, K. Vaitinen, M. Chamarczuk, M. Riedel, and I. Kukkonen, and , the COGITO-MIN Working Group, 2018, From regional seismics to high-resolution resource delineation: Example from the Outokumpu Ore District, Eastern Finland: 80th Annual International Conference and Exhibition, EAGE, Extended Abstracts, Tu 2MIN P04, doi: [10.3997/2214-4609.201802716](https://doi.org/10.3997/2214-4609.201802716).
- Krizhevsky, A., I. Sutskever, and G. E. Hinton, 2012, ImageNet classification with deep convolutional neural networks: Advances in Neural Information Processing Systems, **25**, 1097–1105, doi: [10.1145/3065386](https://doi.org/10.1145/3065386).
- Li, Z., M. A. Meier, E. Hauksson, Z. Zhan, and J. Andrews, 2018a, Machine learning seismic wave discrimination: Application to earthquake early warning: Geophysical Research Letters, **45**, 4773–4779, doi: [10.1029/2018GL077870](https://doi.org/10.1029/2018GL077870).
- Li, Z., Z. Peng, D. Hollis, L. Zhou, and J. McClellan, 2018b, High-resolution seismic event detection using local similarity for large-N-arrays: Scientific Reports, **8**, 1646, doi: [10.1038/s41598-018-19728-w](https://doi.org/10.1038/s41598-018-19728-w).
- Lin, F., D. Li, R. W. Clayton, and D. Hollis, 2013, High-resolution 3D shallow crustal structure in Long Beach, California: Application of ambient noise tomography on a dense seismic array: Geophysics, **78**, no. 4, Q45–Q56, doi: [10.1190/geo2012-0453.1](https://doi.org/10.1190/geo2012-0453.1).
- McNamara, E. D., C. R. Hutt, L. S. Gee, H. M. Benz, and R. P. Buland, 2009, A method to establish seismic noise baselines for automated station assessment: Seismological Research Letters, **80**, 628–637, doi: [10.1785/gssrl.80.4.628](https://doi.org/10.1785/gssrl.80.4.628).
- Melo, G., A. Malcolm, D. Mikesell, and K. van Wijk, 2013, Using SVD for improved interferometric Green's function retrieval: Geophysical Journal International, **194**, 1596–1612, doi: [10.1093/gji/ggt172](https://doi.org/10.1093/gji/ggt172).
- Meunier, J., 2011, Seismic acquisition from yesterday to tomorrow: SEG.
- Moreau, L., L. Stehly, P. Boué, Y. Lu, E. Larose, and M. Campillo, 2017, Improving ambient noise correlation functions with an SVD-based Wiener filter: Geophysical Journal International, **211**, 418–426, doi: [10.1093/gji/ggx306](https://doi.org/10.1093/gji/ggx306).
- Nakata, N., and G. C. Beroza, 2017, Towards a high-resolution velocity model with a very dense array at Diablo Canyon, California: Poster Presentation, SCEC Annual Meeting.
- Nakata, N., P. Boué, F. Brenguier, P. Roux, V. Ferrazzini, and M. Campillo, 2016, Body and surface wave reconstruction from seismic noise correlations between arrays at Piton de la Fournaise volcano: Geophysical Research Letters, **43**, 1047–1054, doi: [10.1002/2015GL066997](https://doi.org/10.1002/2015GL066997).
- Nakata, N., J. P. Chang, J. F. Lawrence, and P. Boue, 2015, Body wave extraction and tomography at Long Beach, California, with ambient-noise interferometry: Journal of Geophysical Research: Solid Earth, **120**, 1159–1173, doi: [10.1002/2015JB011870](https://doi.org/10.1002/2015JB011870).
- Nishitsuji, Y., E. Ruigrok, M. Gómez, and D. Draganov, 2014, Global-phase H/V spectral ratio for imaging the basin in the Malargüe region, Argentina: Seismological Research Letters, **85**, 1004–1011, doi: [10.1785/0220140054](https://doi.org/10.1785/0220140054).
- Olivier, G., F. Brenguier, M. Campillo, R. Lynch, and P. Roux, 2015, Body-wave reconstruction from ambient noise seismic noise correlations in an underground mine: Geophysics, **80**, no. 3, KS11–KS25, doi: [10.1190/geo2014-0299.1](https://doi.org/10.1190/geo2014-0299.1).
- Olivier, G., J. Chaput, and B. Borchers, 2018, Using supervised machine learning to improve active source signal retrieval: Seismological Research Letters, **89**, 1023–1029, doi: [10.1785/0220170239](https://doi.org/10.1785/0220170239).
- Panea, I., D. Draganov, C. A. Vidal, and V. Mocanu, 2014, Retrieval of reflections from ambient noise recorded in the Mizil area, Romania: Geophysics, **79**, no. 3, Q31–Q42, doi: [10.1190/geo2013-0292.1](https://doi.org/10.1190/geo2013-0292.1).
- Pedregosa, F., G. Varoquaux, A. Gramfort, V. Michel, B. Thirion, O. Grisel, M. Blondel, P. Prettenhofer, R. Weiss, and V. Dubourg, 2011, Scikit-learn: Machine learning in Python: Journal of Machine Learning Research, **12**, 2825–2830.
- Quiros, A. D., L. D. Brown, K. K. Davenport, J. A. Hole, A. Cabolova, C. Chen, L. Han, M. C. Chapman, and W. D. Mooney, 2017, Reflection imaging with earthquake sources and dense arrays: Journal of Geophysical Research, **122**, 3076–3098, doi: [10.1002/2016JB013677](https://doi.org/10.1002/2016JB013677).
- Quiros, A. D., L. D. Brown, and D. Kim, 2016, Seismic interferometry of railroad induced ground motions: Body and surface wave imaging: Geophysical Journal International, **205**, 301–313, doi: [10.1093/gji/ggw033](https://doi.org/10.1093/gji/ggw033).
- Reshetnikov, A., S. Buske, and S. A. Shapiro, 2010, Seismic imaging using microseismic events: Results from the San Andreas fault system at SAFOD: Journal of Geophysical Research: Solid Earth, **115**, B12324, doi: [10.1029/2009JB007049](https://doi.org/10.1029/2009JB007049).
- Roots, E., A. Calvert, J. A. Calvert, and J. Craven, 2017, Interferometric seismic imaging around the active Lalor mine in the Flin Flon greenstone belt, Canada: Tectonophysics, **718**, 92–104, doi: [10.1016/j.tecto.2017.04.024](https://doi.org/10.1016/j.tecto.2017.04.024).
- Rost, S., and C. Thomas, 2002, Array seismology: Methods and applications: Review of Geophysics, **40**, 1008, doi: [10.1029/2000RG000100](https://doi.org/10.1029/2000RG000100).
- Roux, P., L. Moreau, A. Lecointre, G. Hillers, M. Campillo, Y. Ben-Zion, D. Zigone, and F. Vernon, 2016, A methodological approach towards high-resolution surface wave imaging of the San Jacinto Fault Zone using ambient-noise recordings at a spatially dense array: Geophysical Journal International, **206**, 980–992, doi: [10.1093/gji/ggw193](https://doi.org/10.1093/gji/ggw193).
- Ruigrok, E., D. Draganov, M. Gómez, J. Ruzzante, D. Torres, I. López Pumarega, N. Barbero, A. Ramires, A. R. Castaño Gañan, K. van Wijk, and K. Wapenaar, 2012, Malargüe seismic array: Design and deployment of the temporary array: The European Physical Journal Plus, **127**, 10, doi: [10.1140/epjp/i2012-12126-7](https://doi.org/10.1140/epjp/i2012-12126-7).
- Shelly, D. R., G. C. Beroza, and S. Ide, 2007, Non-volcanic tremor and low-frequency earthquake swarms: Nature, **446**, 305–307, doi: [10.1038/nature05666](https://doi.org/10.1038/nature05666).
- Smola, A. J., and B. Schölkopf, 2004, A tutorial on support vector regression: Statistics and Computing, **14**, 199–222, doi: [10.1023/B:STCO.0000035301.49549.88](https://doi.org/10.1023/B:STCO.0000035301.49549.88).
- Trad, D., 2009, Five-dimensional interpolation: Recovering from acquisition constraints: Geophysics, **74**, no. 6, V123–V132, doi: [10.1190/1.3245216](https://doi.org/10.1190/1.3245216).
- Van der Neut, J., D. Draganov, and C. Almagro Vidal, 2011, Diagnosing virtual source radiation characteristics without a velocity model: 73rd Annual International Conference and Exhibition, EAGE, Extended Abstracts, P377, doi: [10.3997/2214-4609.20149640](https://doi.org/10.3997/2214-4609.20149640).
- Vapnik, V. N., 1998, Statistical learning theory: Wiley-Interscience.
- Yoon, C. E., O. O'Reilly, K. J. Bergen, and G. C. Beroza, 2015, Earthquake detection through computationally efficient similarity search: Science Advances, **1**, e1501057, doi: [10.1126/sciadv.1501057](https://doi.org/10.1126/sciadv.1501057).
- Zhang, Y., Y. E. Li, H. Zhang, and T. Ku, 2018, Near-surface site investigation by seismic interferometry using urban traffic noise in Singapore: Geophysics, **84**, no. 2, B169–B180, doi: [10.1190/geo2017-0798.1](https://doi.org/10.1190/geo2017-0798.1).